



## Testing gravity with cold-atom interferometers

G. W. Biedermann,<sup>\*</sup> X. Wu, L. Deslauriers, S. Roy, C. Mahadeswaraswamy, and M. A. Kasevich<sup>†</sup>  
*Physics Department, Stanford University, Stanford, California 94305, USA*

(Received 1 December 2014; published 24 March 2015)

We present a horizontal gravity gradiometer atom interferometer for precision gravitational tests. The horizontal configuration is superior for maximizing the inertial signal in the atom interferometer from a nearby proof mass. In our device, we have suppressed spurious noise associated with the horizontal configuration to achieve a differential acceleration sensitivity of  $4.2 \times 10^{-9} \text{ g}/\sqrt{\text{Hz}}$  over a 70-cm baseline or  $3.0 \times 10^{-9} \text{ g}/\sqrt{\text{Hz}}$  inferred per accelerometer. Using the performance of this instrument, we characterize the results of possible future gravitational tests. We demonstrate a statistical uncertainty of  $3 \times 10^{-4}$  for a proof-of-concept measurement of the gravitational constant that is competitive with the present limit of  $1.2 \times 10^{-4}$  using other techniques. From this measurement, we provide a statistical constraint on a Yukawa-type fifth force at  $8 \times 10^{-3}$  near the poorly known length scale of 10 cm. Limits approaching  $10^{-5}$  appear feasible. We discuss improvements that can enable uncertainties falling well below  $10^{-5}$  for both experiments.

DOI: [10.1103/PhysRevA.91.033629](https://doi.org/10.1103/PhysRevA.91.033629)

PACS number(s): 37.25.+k, 06.30.Gv, 04.80.Cc, 06.20.Jr

### I. INTRODUCTION

Light-pulse atom interferometers demonstrate exceptional inertial sensitivity. The nature of their construction lends long-term stability and intrinsic accuracy, making them compelling candidates for advancing our knowledge of gravitational physics. Recent work has shown the promise of this technology in a precision measurement of the gravitational constant [1,2] as well as precision gradiometry [3], single-atom-force sensors [4], and navigation sensors [5–9]. New experiments aim to test the weak equivalence principle by measuring the differential acceleration between atom species in a dual-species accelerometer [10,11], and future missions are being developed to deploy space-based gravity wave detectors [12].

The weakness of the gravitational coupling presents a significant challenge for precision measurements of gravitational forces. The 2010 CODATA values  $G$  with a relative standard uncertainty of  $1.2 \times 10^{-4}$  [13]. If taken as a steady trend, the uncertainty has improved by only 1 order of magnitude per century since the first measurements of  $G$  by Cavendish in 1798 [14]. High-accuracy measurements following the first CODATA adjustment in 1986 disagreed with each other at the  $10^{-3}$  level, though their accuracies exceeded  $10^{-4}$  [15]. New understandings of systematic shifts in these measurements [16] and subsequent precision measurements have led to the improved precision on  $G$  in 2010. Therefore an independent evaluation of  $G$  is welcome for determining the true value of  $G$  with greater accuracy. In this paper, we present an atom interferometer that offers a contribution to this endeavor with a forecast precision well below  $10^{-5}$ .

In a related manner, inextricably linked are the precision of these measurements and the exploration of the dependence of gravity on the spatial separation of the participating test masses. A myriad of theories predict departures from the inverse square law (ISL) model just below the resolution of current experiments [17]. These theories often predict the

existence of a new force mediated by a massive particle exhibiting a characteristic range of  $\lambda = \hbar/m_\gamma c$ , where  $m_\gamma$  is the particle mass. In this case, the gravitational force would arise from a Yukawa potential of the form

$$U(r) = -\frac{Gm_1m_2}{r}(1 + \alpha e^{-r/\lambda}), \quad (1)$$

where  $\alpha$  is the coupling strength,  $m_1$  and  $m_2$  are the two participating masses, and  $r$  is the spatial separation of the masses. The work shown here offers the possibility to constrain  $\alpha$  near  $10^{-5}$  for  $\lambda \sim 10$  cm for an improvement of  $10^2$  over current limits [18–20].

In this paper we present preliminary gravity tests using our technique with two experiments: a determination of the statistical uncertainty for a measurement of the gravitational constant and a forecast of a statistical constraint upon a putative Yukawa-type fifth force. Our promising results motivate further work to realize the full potential of this approach. In the remainder of this paper we first discuss the atom interferometer measurement, including the theoretical treatment along with our measurement technique in Sec. II. We then describe the apparatus and the current sensitivity in Sec. III, followed by a characterization of the atom interferometer performance in Sec. IV. Our evaluation of the statistical uncertainty for a measurement of  $G$  is found in Sec. V A, and a forecast of a constraint upon the Yukawa potential is found in Sec. V B.

### II. ATOM INTERFEROMETER MEASUREMENT

The experiment measures acceleration using a pulsed-light,  $\pi/2$ - $\pi$ - $\pi/2$  atom interferometer [21]. The functional principle of the interferometer can be understood with a simple model. This model encapsulates much of the behavior exhibited by the measurement process while neglecting several small, yet important nuances, such as the effect of magnetic fields, large local gradients in gravity, and wave-packet overlap, as discussed below.

Consider the case of a test mass undergoing constant acceleration. A measurement of the position of the mass at three equispaced points in time defines the curvature or

<sup>\*</sup>Present address: Sandia National Laboratories, Albuquerque, New Mexico 87123, USA.

<sup>†</sup>kasevich@stanford.edu

acceleration associated with its path as

$$a = \frac{x_1 - 2x_2 + x_3}{T^2}, \quad (2)$$

where  $T$  is the time between successive position measurements  $x_i$ . For the atom interferometer, the test mass is the cesium atom and the position measurements are referenced to a pulsed, resonant optical field where the optical phase fronts act as the ticks of a ruler. If this optical field is referenced to a stable frame, then the final interferometer phase shift reveals the acceleration of the atom with respect to that frame along the direction defined by the light propagation. Contributions from a constant velocity vanish in Eq. (2).

The detailed theory of light pulse atom interferometry is available in Refs. [22] and [23]. In brief, to perform these measurements, we interrogate the atoms with a velocity-sensitive, two-photon stimulated Raman transition coupling the  $6S_{1/2}$ ,  $F = 3$ , and  $F = 4$  hyperfine ground states of atomic cesium. These transitions imprint the optical phase associated with the Raman coupling onto the phase difference of the hyperfine ground-state atomic wave functions. This phase is a measure of the atom's position during the Raman pulse. In the limit of short, resonant pulses, the transition rules between these two states take a simple form of

$$\begin{aligned} |3, \mathbf{p}\rangle &\rightarrow e^{i\phi(t)} |4, \mathbf{p} + \hbar\mathbf{k}_{\text{eff}}\rangle \\ |4, \mathbf{p} + \hbar\mathbf{k}_{\text{eff}}\rangle &\rightarrow e^{-i\phi(t)} |3, \mathbf{p}\rangle, \end{aligned} \quad (3)$$

where  $\phi(t) = \mathbf{k}_{\text{eff}} \cdot \mathbf{x}(t)$ . Here  $\mathbf{x}(t)$  is the mean position of the wave packet at the pulse time  $t$ ,  $\mathbf{p}$  is the mean atom momentum, and  $\mathbf{k}_{\text{eff}}$  is the Raman wave vector defined by  $\mathbf{k}_{\text{eff}} = \mathbf{k}_1 - \mathbf{k}_2$ , where  $\mathbf{k}_1$  and  $\mathbf{k}_2$  are the wave vectors of two counterpropagating Raman beams. Conservation of momentum dictates that the atomic momentum change by  $\hbar\mathbf{k}_{\text{eff}}$  for an atom undergoing a Raman transition. This amounts to a velocity change of  $\approx 7$  mm/s in our experiment, which leads to a macroscopic wave-packet separation of 0.6 mm over the duration of the interferometer, which is 170 ms in this work.

These Raman pulses drive coherent Rabi oscillations between the  $F = 3$  and  $F = 4$  ground states. The pulses are characterized by the pulse area, defined here as  $\Theta \equiv \Omega_R \tau_p$ , where  $\Omega_R$  is the Rabi frequency, which is assumed to be constant, and  $\tau_p$  is the duration of the pulse. As an example, for an atom initially in  $F = 3$ , a  $\Theta = \pi/2$  pulse leaves the atom in an equal superposition of  $F = 3$  and  $F = 4$ , analogous to an optical beam splitter. It follows that a  $\Theta = \pi$  pulse transfers an atom in  $F = 3$  to  $F = 4$  (and vice versa), corresponding to a mirror. Therefore a  $\pi/2$ - $\pi$ - $\pi/2$  pulse sequence creates a Mach-Zehnder style atom interferometer by splitting, redirecting, and then recombining the atom wave packets. In practice, we employ an atomic fountain to loft atoms vertically upward and apply  $\mathbf{k}_{\text{eff}}$  in the lateral direction (see Fig. 1). The force of earth's gravitational pull causes the atoms to arc in a parabolic trajectory, returning them to the launch position such that they are in free fall for the entire duration of the interferometer.

Each aforementioned position measurement is encapsulated in the phase  $\phi(t)$ . Using the rules in Eq. (3) for a  $\pi/2$ - $\pi$ - $\pi/2$  interferometer, the transition amplitude for an atom beginning in state  $F = 3$  is

$$P(|4, \mathbf{p} + \hbar\mathbf{k}_{\text{eff}}\rangle) = \frac{1}{2} [1 - \cos(\Delta\phi)], \quad (4)$$

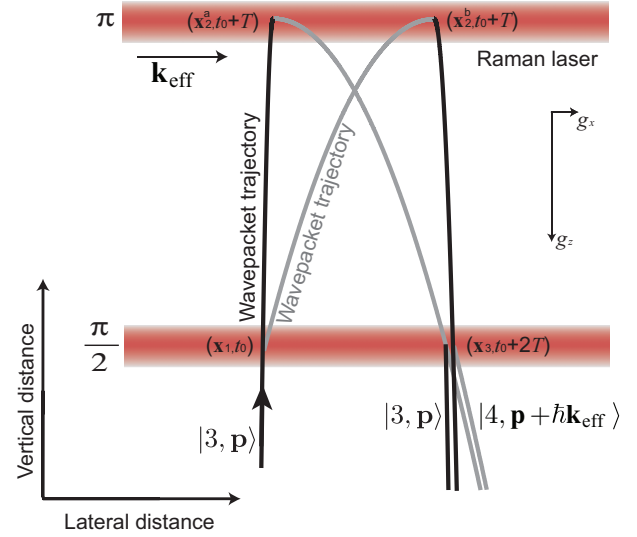


FIG. 1. (Color online) Interferometer recoil diagram in an atomic fountain with a gravity gradient. The prepared wave packet,  $|3, \mathbf{p}\rangle$ , interacts with the first  $\pi/2$  pulse and splits in the lateral direction into a coherent superposition of states  $|3, \mathbf{p}\rangle$  and  $|4, \mathbf{p} + \hbar\mathbf{k}_{\text{eff}}\rangle$  while ascending to the apex of the trajectory. At the apex the wave packets are redirected back toward one another by the  $\pi$  pulse. The final  $\pi/2$  pulse recombines the wave packets near the original launch location. The direction of  $\mathbf{k}_{\text{eff}}$  determines that the interferometer measures  $g_x$ , the lateral acceleration.

where

$$\Delta\phi = \phi_1 - \phi_2^a - \phi_2^b + \phi_3, \quad (5)$$

in analogy to Eq. (2). Here  $\phi_i^j$  indicates the phase acquired during the  $i$ th pulse for path  $j$ . For an atom in a uniform gravitational field it follows that

$$\Delta\phi = -\mathbf{k}_{\text{eff}} \cdot gT^2 + \Delta\phi_0, \quad (6)$$

where  $g$  is the local acceleration due to gravity,  $T$  is the time between interferometer pulses, and  $\Delta\phi_0$  is an offset phase which vanishes when the measurement is referenced to a stable frame.

Additional effects contribute to the overall interferometer phase shift. These include the phase evolution of the wave packets in the two interferometer arms according to the Feynman path integral approach [24], as well as a phase shift arising from imperfect overlap of these wave packets following the final  $\pi/2$  pulse. These contributions are small relative to the light phase shift yet are important for high-accuracy metrology and are detailed in Refs. [23] and [1].

### III. APPARATUS

Two simultaneous acceleration measurements at different spatial locations typically constitute a gravity gradiometer. Such a measurement approximates the spatial rate of change in the gravity field. Accordingly, our gradiometer employs two spatially separated gravimeters based on atom interferometry. Each gravimeter is configured to measure the lateral component of gravity and the gravimeters are as well spatially separated in the lateral direction (see Fig. 2). A key feature

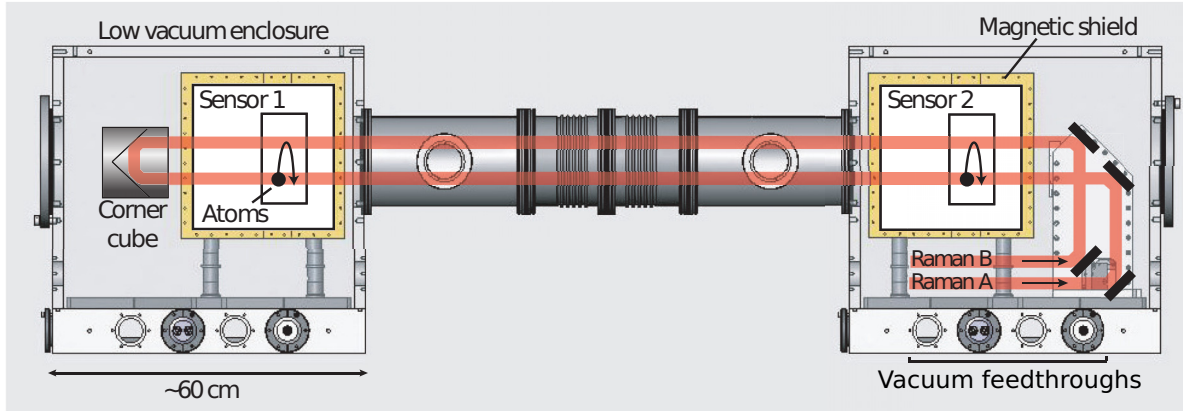


FIG. 2. (Color online) A scaled schematic of the Raman laser delivery in the experiment. (Note that the sensor separation is reduced for the gravitational tests.) The Raman light enters the low-vacuum enclosure through optical fiber vacuum feedthroughs. Two collimated Raman beams counterpropagate in free space through both sensors and reflect from a corner cube, giving two tiers for optical excitation. The schematic shows the relative locations of the two UHV chambers in which the atom interferometers occur. The fountain trajectories are exaggerated horizontally to depict motion.

of this technique is that both gravimeters are interrogated with a common measurement laser, which ideally propagates undisturbed between the gravimeters. Since both gravimeters reference this laser, common mode platform noise is highly suppressed in the differential acceleration measurement, as discussed below.

Each gravimeter is a compact package with supporting optomechanical hardware densely arranged around an independent ultrahigh-vacuum chamber of  $<10^{-9}$  Torr [25]. This package is surrounded by two layers of magnetic shielding to isolate the measurement. To eliminate spurious noise associated with beam steering as discussed below, the entire gradiometer is enclosed in a low-vacuum chamber of  $\approx 50$  mTorr. The structure of the low-vacuum chamber is carefully designed using finite-element analysis to avoid significant misalignment of the Raman beams due to the large forces experienced by the structure from evacuation.

Using atomic fountain techniques, we prepared a  $2.3\text{-}\mu\text{K}$  [26],  $3\text{-mm}$   $1/e^2$  radius cloud of  $\approx 10^8$  cesium atoms in the  $6S_{1/2}F = 3, m_f = 0$  hyperfine ground state moving upward at  $1\text{ m/s}$ . The atoms are in darkness during the fountain, except for three temporally separated pulses of resonant Raman light which interrogate the trajectory as previously described. Following the interferometer, the atoms return back to approximately the same location from which they were launched. At this point acceleration information is encoded in the probability distribution between the two ground states. In order to determine these two populations, and thus the probability distribution, we project the superposition and spatially separate the atoms according to their state with radiation pressure. We then measure the respective populations of the two states with a simultaneous fluorescence detection technique described in Ref. [27]. Counting the number of atoms in both states enables the computation of a normalized transition probability to  $|F = 4\rangle$ ,  $P_{F=4} = N_4/(N_4 + N_3)$ , where  $N_i$  is the number of atoms measured in state  $|F = i\rangle$ . This immunizes the result against shot-to-shot atom number fluctuations. An alternative use of this apparatus as an atomic clock is presented in [28].

Due to the equivalence principle, it is impossible to distinguish between acceleration of the atoms and the reference mirror. In practice, platform vibrations cause spurious phase shifts [ $\Delta\phi_0 \neq 0$  in Eq. (6)], which severely limit the measurement sensitivity if not properly controlled [29]. In the present setup, this noise randomizes the phase of the interferometer at levels larger than  $\pi$  radians. However, our instrument uses two interferometers that share this noise in common such that the difference phase is preserved with high fidelity. Plotting the two transition amplitudes parametrically (see Fig. 3) reveals a well-defined phase relationship between the sinusoidal outputs of the two interferometers characterized by the ellipticity [30]. Accordingly, we use ellipse-specific fitting to determine the differential phase and therefore the differential acceleration signal between the two sensors as discussed further in Sec. IV.

The Raman laser is sourced from a cavity-locked diode laser. This system consists of a New Focus Vortex 6017 laser locked to an optical cavity via the Pound-Drever-Hall technique [31]. The cavity is built from low-expansion Zerodur and has a hemispherical mirror geometry with a  $10\text{-cm}$  separation and a finesse of 8000. The cavity length is piezo-controlled and in this manner locked to a Cs resonance to eliminate drift and reduce low-frequency acoustic noise. The cavity output has a linewidth of  $\approx 15\text{ kHz}$ , and calculations show that the gradiometer noise floor associated with this laser is below the current sensitivity, as is discussed below.

The scrubbed output from the cavity is fiber coupled and routed into the vacuum enclosures after further amplification and frequency control. We use Photline fiber modulators to generate the required  $9.1926\text{-GHz}$  hyperfine splitting frequency difference between the two counterpropagating Raman beams. The final amplification is performed inside the low-vacuum enclosure with an Eagleyard tapered amplifier. The tapered amplifier output is spatially filtered and then collimated to a radius of  $r_{1/e} = 6\text{ mm}$ . We achieve an intensity of  $\approx 100\text{ mW/cm}^2$  per beam with a single-photon detuning of  $670\text{ MHz}$  blue of the  $|6P_{3/2}, F' = 5\rangle$  resonance, resulting in a two-photon Rabi frequency of  $\Omega_R = 2\pi \times 100\text{ kHz}$ . These two beams are routed through a periscope and the two-level

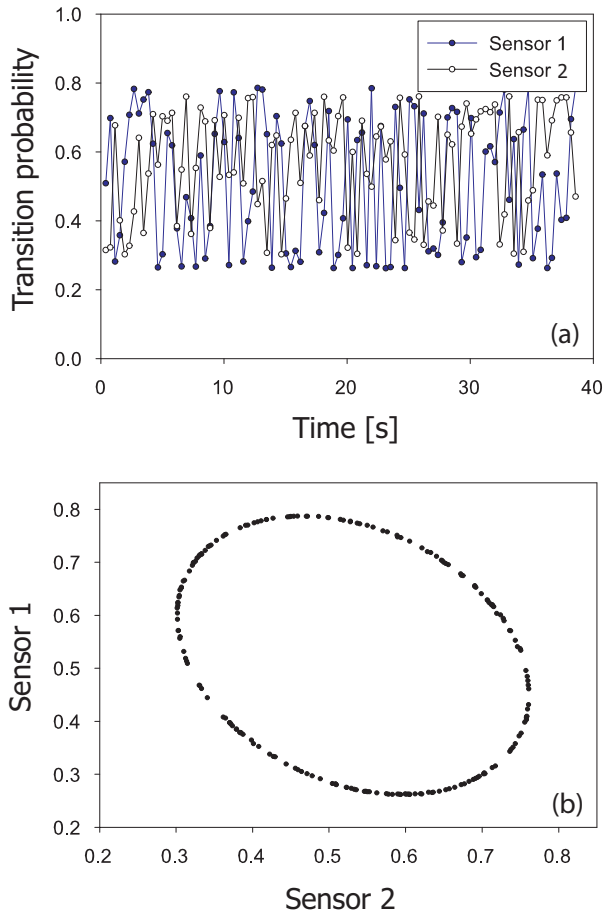


FIG. 3. (Color online) (a) An example of the measured normalized transition probability  $P_{F=4}$  of the two interferometers, sensor 1 and sensor 2, which comprise the gradiometer. Common-mode noise in the optical delivery system masks the phase information in the individual sensors while the difference phase is preserved. (b) Common-mode acceleration noise is suppressed when the normalized transition probabilities of sensor 1 and sensor 2 are plotted parametrically. 200 data points form this example of a low-phase-noise ellipse. The shot-to-shot fluctuations of the phase readout indicate a noise of 1.6 mrad per 20-point ellipse.

Raman beam configuration shown in Fig. 2. A corner cube reflector (PLX HM-25-1G) guarantees the parallelism of the two beam levels to within  $5 \mu\text{rad}$ , which is essential for good interferometer contrast. In this configuration, the atoms interact with the first  $\pi/2$  pulse immediately after the launch via the lower beam tier. The second pulse ( $\pi$  pulse) is applied with the upper beam tier at the apex of the fountain, and the final  $\pi/2$  pulse again uses the lower tier as the atoms travel down to the detection region. A crossed linear polarization Raman excitation geometry is used to reduce susceptibility to parasitic reflections, which give rise to standing-wave ac Stark noise.

Using this apparatus, we observe continuous time records with a short-term phase noise of  $3.1 \text{ mrad}/\sqrt{\text{Hz}}$  inferred per interferometer. For our system parameters, this corresponds to a differential acceleration sensitivity of  $4.2 \times 10^{-9} \text{ g}/\sqrt{\text{Hz}}$  or  $3.0 \times 10^{-9} \text{ g}/\sqrt{\text{Hz}}$  inferred per accelerometer. It is noteworthy that Bayesian techniques can be applied to the ellipse phase

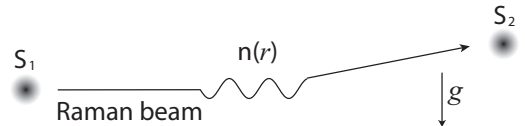


FIG. 4. Index of refraction variations in the air between the sensors ( $S_1$  and  $S_2$ ) result in an angular deviation of the Raman beam. Stochastic variations cause shot-to-shot fluctuations in the differential projection of the two measurement axes onto  $g$ , which limits sensitivity if not properly controlled.

estimation routine to reduce the noise and systematic offset associated with simple ellipse fitting [32].

Although many parameters are explored to achieve this performance, two key experimental factors bear discussion here: intersensor beam steering effects and Raman laser frequency stability. Perturbations to the Raman beam between the sensors produce a differential projection of each sensor's measurement axis onto  $g$  (see Fig. 4). Considering that  $|\mathbf{k}_{\text{eff}}|g_z T^2 \approx 10^6 \text{ rad}$

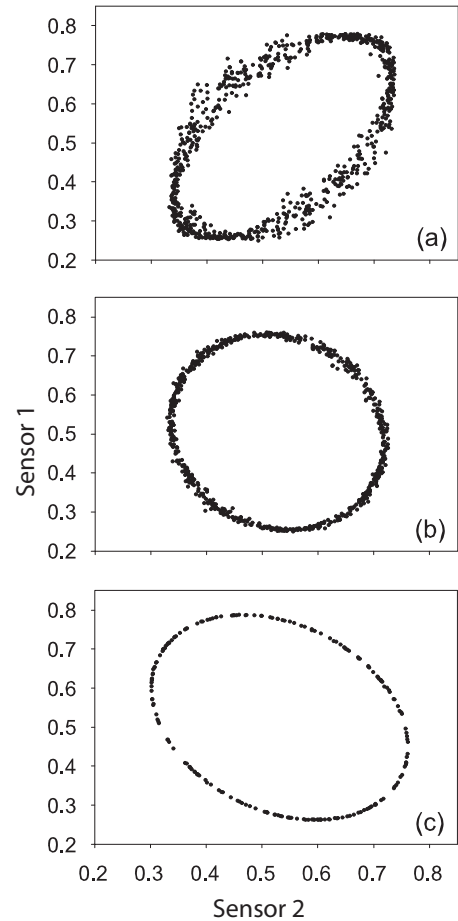


FIG. 5. Ellipse plots representing key noise limits. The normalized transition probabilities,  $P_{F=4}$ , of sensor 1 and sensor 2 are plotted parametrically for three exemplary cases: (a) typical data with air between the sensors, giving a differential phase noise of  $190 \text{ mrad}/\sqrt{\text{Hz}}$ ; (b) typical data after evacuating the air but generating the Raman beams with a DBR diode laser, giving a differential phase noise of  $38 \text{ mrad}/\sqrt{\text{Hz}}$ , and (c) typical data using a cavity-locked laser, giving a differential phase noise of  $4.4 \text{ mrad}/\sqrt{\text{Hz}}$ .

for typical instrument parameters, it is clear that beam steering at the mrad level will produce mrad interferometer phase shifts, commensurate with the device noise floor. We find that in practice, stochastic index of refraction variations in the air between the sensors pose a severe limitation for horizontal gradient measurements such as this where  $\mathbf{k}_{\text{eff}}$  is perpendicular to  $g$  [see Fig. 5(a)]. In our system, this effect limits the differential phase noise to  $>190 \text{ mrad}/\sqrt{\text{Hz}}$ . Although phase readout below 1 mrad is routine in optical interferometers [33], heat sources in our apparatus such as magnetic field coils frustrate conventional solutions. We find that enclosing the entire gradiometer in a low-vacuum chamber eliminates the associated differential phase noise.

To a lesser degree, we find that Raman laser frequency noise limits the differential phase noise, as shown in Ref. [3] and later in Ref. [34]. To illustrate this effect, consider that a discrete laser frequency change for one interferometer pulse results in a phase error of  $\delta\phi = 4\pi\delta\nu L/c$ , where  $\delta\nu$  is the laser frequency change,  $c$  is the speed of light, and  $L$  is the separation distance of the two interferometers. We have measured that for a midinterferometer frequency jump of 1.161 MHz, a phase jump of 71.57 mrad results, corresponding to an optical path length of  $L = 72.29 \pm 0.09 \text{ cm}$  after accounting for the effect of the vacuum windows. This agrees with our physical measurement of  $72.39 \pm 0.25 \text{ cm}$ . In general, the interferometer phase noise is a function of the laser frequency noise spectrum up to a cutoff frequency commensurate with the Rabi frequency [34]. We find that sourcing the Raman laser with a  $\delta\nu \approx 1 \text{ MHz}$  linewidth distributed Bragg reflector (DBR) diode limits the differential phase noise to  $38 \text{ mrad}/\sqrt{\text{Hz}}$ , as shown in Fig. 5(b). In contrast, a  $\delta\nu \approx 15 \text{ kHz}$  linewidth cavity-locked laser enables a noise of  $3.1 \text{ mrad}/\sqrt{\text{Hz}}$  inferred per interferometer [see Fig. 5(c)]. Calculations show that this cavity-laser performance is not a limit for the current device performance.

#### IV. GRADIOMETER SENSITIVITY

In this section, we present the current performance of the gradiometer including an evaluation of short- and long-term noise performance. As previously discussed, the highly common-mode noise shared by the interferometers allows the use of ellipse-specific fitting to extract the differential phase signal between the two interferometers. In our experiment, an optimal fit is typically achieved with 20 data points. For a larger sample, the fit gains a susceptibility to slight drifts in detection offsets and interferometer phase during the collection of the ellipse points, which typically takes 8 s for the 20 points. We find that more than ten points are needed to achieve a good fit and at times corresponding to more than 100 points, system drifts degrade the ellipse fit performance.

We determine the short-term sensitivity of the interferometers from the rms of a double,  $3\sigma$  outlier cut on a version of the time record with drift removed as briefly elaborated here. We log a time record of the ellipse phase values with 20 points per ellipse and calculate the mean values of successive groupings of 20 ellipse phases. We subtract the slow drift from the original time record using a shape-preserving piecewise cubic interpolation of the mean value time record. We calculate the rms of this smoothed record to reveal  $3\sigma$  outliers that we

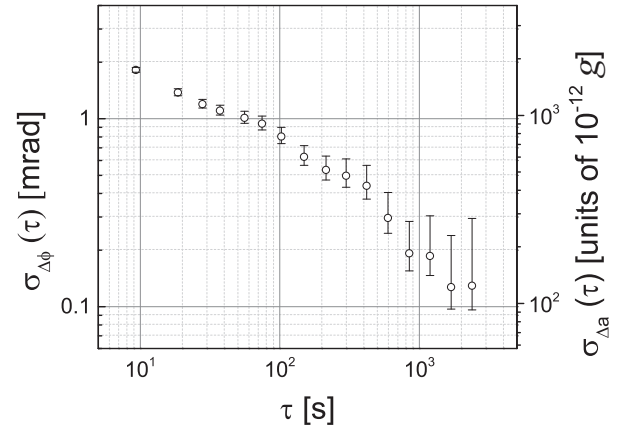


FIG. 6. An Allan deviation analysis of the phase stability from the differential acceleration measurement shows that the system can integrate as white noise for periods of  $2.5 \times 10^3 \text{ s}$ . Here 0.1 mrad corresponds to  $96 \times 10^{-12} \text{ g}$ . No attempt is made to correlate the data with system environmental parameters.

then remove. We then smooth the resultant data set a second time following the same procedure and again remove  $3\sigma$  outliers. This protects the smoothing routine from the effects of very large outliers, and the second cut removes much fewer points than the first.

With this technique we observe continuous time records with a short-term noise of 1.6 mrad per ellipse. In this case  $T = 85 \text{ ms}$  and our repetition rate was 2.55 Hz, giving a differential acceleration sensitivity of  $4.2 \times 10^{-9} \text{ g}/\sqrt{\text{Hz}}$  or  $3.0 \times 10^{-9} \text{ g}/\sqrt{\text{Hz}}$  inferred per accelerometer. The long-term performance shows white noise averaging for  $2 \times 10^3 \text{ s}$  (see Fig. 6). Electronic noise and noise caused by intensity and frequency fluctuations of the detection laser are negligible. The long-term noise is likely caused by environmental factors such as temperature drift.

#### V. GRAVITATIONAL TESTS

In this section we explore the suitability of the device for gravitational tests using a laboratory source mass. We first show the instrument's viability for a measurement of  $G$  with a precision approaching  $10^{-4}$ . Second, we interpret this measurement as a test of the inverse-square law. In both cases we provide an outlook for future gravity tests using atom interferometers.

##### A. Gravitational constant

In our measurement of the gravitational signal, we take advantage of a symmetric source mass configuration to reduce sensitivity to atom-source positioning (see Fig. 7). Relative positioning of the source mass and atoms is a significant source of error in previous measurements of  $G$  using atom interferometry [1]. By placing the source mass between the sensors, we make second-order the dependence of the field on source position deviations along  $\hat{x}$ . For technical reasons, our experiment is performed with a small asymmetry in the distance of the two sensors from the source masses. This does not inhibit the present demonstration, as calculations show that

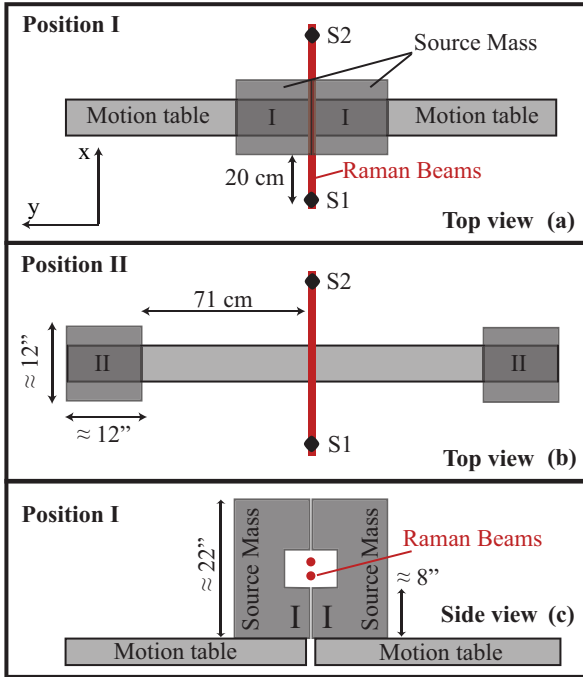


FIG. 7. (Color online) Mass-sensor configuration for  $G$  measurement where  $S1$  and  $S2$  are the positions of the atom interferometer ensembles. The source masses are chopped between positions I and II, subfigures (a) and (b), respectively. A side view is shown in (c), depicting the  $\approx 8''$  horizontal by  $\approx 6''$  vertical opening to allow Raman beam propagation between the sensors.

our position repeatability of  $<5 \mu\text{m}$  is sufficient for a precision approaching  $10^{-5}$ , nor do the results indicate the presence of any slow drifts in the mass signal.

In the setup shown in Fig. 7, each of the two 540-kg source masses consists of 45 securely stacked laboratory lead bricks ( $2'' \times 4'' \times 8''$ ) strapped firmly to a LinTech 174630 precision positioning table. The positioning system enables rapid relocation of the source mass between the two end points or a 70-cm travel in less than 8 s. The table, motors, and drivers are specifically chosen to manage the torque and linear accelerations required for this motion profile. The positioning achieves this repeatability with simple mechanical limit switches at either end triggered by sloped flags. These switches are approached slowly at  $\approx 1 \text{ mm/s}$  to avoid overshoot due to the large inertia of the system. To modulate the gravitational field, the source masses are chopped between positions I and II at regular intervals (see Fig. 7). The signal at each position is averaged for 40 s, which is empirically chosen to minimize the introduction of noise from slow drifts in the gradiometer phase. The mass motion is synchronized with the interferometer timing system and data collection procedure.

Using the technique described above, we measure the signal associated with modulating the gravity field between two values, giving a square wave output [see Fig. 8(a)]. Slow, systematic drifts contaminate this signal such that simple subtraction of adjacent values is inadequate to determine the wave amplitude. We use three adjacent values to approximate the local linear rate of drift and largely remove this perturbation. Explicitly, for the  $k$ th value we

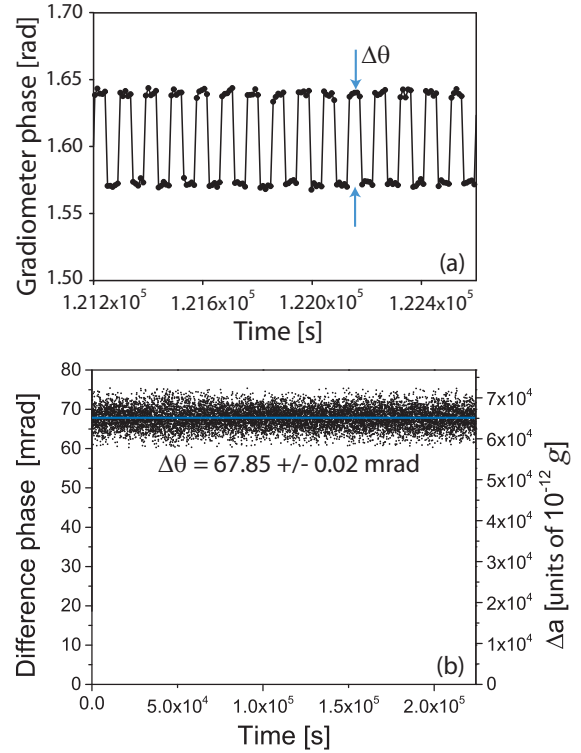


FIG. 8. (Color online) (a) The gravity potential is chopped between two values to remove the sensitivity to long-term drifts in phase. This modulates the differential gravity vector along  $\mathbf{k}_{\text{eff}}$  by  $(64.93 \pm 0.02) \times 10^{-9} g$  at a repetition rate of 0.01 Hz. (b) The difference signal of the chopped gradiometer phase for a 2.6-day averaging interval. The resulting phase shift is determined to be  $\Delta\theta = 67.85 \pm 0.02 \text{ mrad}$ .

report  $\Delta\theta_k = \Phi_i^{II} - \frac{1}{2}(\Phi_i^I + \Phi_{i+1}^I)$ , where  $k = i$ , measurement  $i$  is the average of five consecutive ellipse phase values and the superscript refers to the mass position in Fig. 7. Our simulations show that this analysis underestimates the short-term noise by 13% but does not affect the interpretation of the long-term sensitivity. We remove occasional sections of data that are excessively noisy due to the loss of Raman laser cavity-lock. The resulting time records are concatenated as shown in Fig. 8(b). An Allan deviation of this record (see Fig. 9) reveals that the brick chop signal integrates as  $\tau^{-1/2}$  for  $10^5 \text{ s}$ . Extrapolating the  $\tau^{-1/2}$  trend to the full length of the data set gives a phase resolution on the gravitational square wave of  $\Delta\theta = 67.85 \pm 0.02 \text{ mrad}$ . This is equivalent to a resolution of  $20 \times 10^{-12} g$ . We therefore determine that this system can perform a measurement of the gravitational constant with a precision of  $\delta G/G = 3 \times 10^{-4}$ .

This demonstrates that our system has the potential to produce a measurement of the gravitational constant competitive with the current precision of  $1.2 \times 10^{-4}$  [13]. Achieving atom shot-noise limited sensitivity can enhance this result 20-fold [27]. Using a higher-density material such as tungsten for the source mass, and arranging the source mass closer to the atoms with an optimized source mass geometry as discussed in Sec. VB can increase the signal more than 6-fold. Furthermore, increasing the averaging time to 1 month can improve the result 3-fold. Combining these possibilities, we forecast a precision of  $1 \times 10^{-6}$ . For comparison, an evaluation of the sensitivity

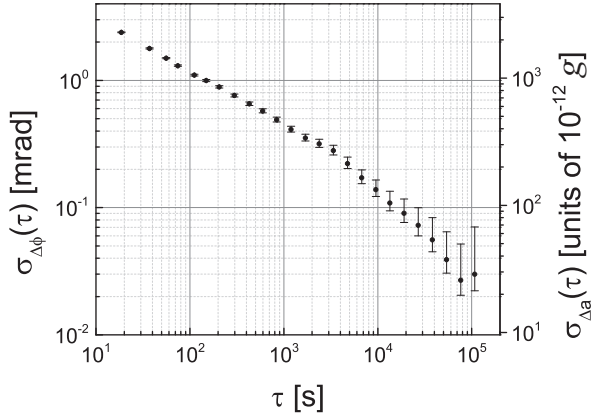


FIG. 9. Allan deviation of the difference phase. The local (three-point) dedrift algorithm results in a signature rise in the signal between  $10^2$  and  $10^4$  s. At longer times, the accuracy of the Allan deviation is restored, giving an uncertainty of  $\pm 0.02$  mrad when extrapolated to the end of the data set, corresponding to  $20 \times 10^{-12}$  g.

of a vertical gradiometer approach for measuring  $G$  [1,2] can be found in [35]. A unique possibility for the horizontal configuration is that the sensitivity can be further enhanced by increasing the interrogation time and extending the vertical dimension of the source mass, giving the potential for an additional order-of-magnitude improvement. Finally, intrinsic sensitivity improvements via large momentum transfer atom optics [36,37] offer avenues for further investigation.

### B. Testing the inverse square law

This experiment may also be configured as a test of Newton's inverse square law by directly measuring the spatial dependence of the gravitational field. In this section we characterize a test that is possible with the current apparatus and then describe an optimized test using upgrades to the sensitivity and the mass configuration.

To place constraints on the strength and length scale of a Yukawa-type force, it is convenient to form ratio quantities in which both the absolute value of the mass as well as the gravitational constant cancel, leaving only the spatial dependence of the force law [38]. This avoids the necessity of comparison with the poorly known value of  $G$  and an absolute mass reference.

In our experiment we measure relative quantities, chopping the test mass between a null reference position and a position of interest, to eliminate slow drifts in the interferometer phase. We therefore construct the ratio

$$\Delta \equiv \frac{(a_1 - a_r) - (a_2 - a_r)}{a_2 - a_r} = \frac{a_1 - a_2}{a_2 - a_r}, \quad (7)$$

where  $a_i$  are acceleration measurements performed at different positions and  $a_r$  is a reference position. In Eq. (7) the numerator and denominator quantities can be considered as two independent measurements with a statistical error equivalent to that described in Sec. V A. Using this measured error, we predict the performance of a Yukawa test with our apparatus by forming the constraint

$$\Delta_Y - \Delta_N \leq \sigma_m, \quad (8)$$

where the subscripts  $Y$  and  $N$  refer to the Yukawa and Newtonian quantities, respectively, and  $\sigma_m$  is calculated using error propagation of the measured  $2\sigma$  precision in Sec. V A or  $40 \times 10^{-12}$  g. We note that this precision was attained with a short, 2.6-day averaging duration which can in principle be increased.

We carefully choose the positions of the three measurements in order to optimize the constraint. The reference measurement  $a_r$  is taken at position II noted in Fig. 7, while  $a_1$  is taken at position I. The optimal constraint on  $\alpha$  occurs when  $(a_2 - a_r) = (a_1 - a_2)$ . This equates to locating the intermediate point  $a_2$  at  $\Delta y = 21$  cm offset from position I, which gives roughly half of the acceleration signal when compared to  $a_1$ . Note that in this prediction the demonstrated experimental precision is reasonably assumed to hold at an intermediate point.

For a Yukawa force, the acceleration is given by

$$a_i = \frac{Gm}{r_i^2} [1 + \alpha e^{-r_i/\lambda} (1 + r_i/\lambda)]. \quad (9)$$

Using this, Eq. (8) may be solved for  $\alpha$  to determine an ISL constraint. However, due to our complicated source mass geometry, we numerically evaluate the terms in Eq. (8) for comparison with the value of  $\sigma_m$  implied by our precision. Specifically, in our experiment the Yukawa acceleration is given by

$$a_x^Y = \sum_i \frac{Gm_i x_i}{r_i^3} \left[ 1 + \alpha e^{-r_i/\lambda} \left( 1 + \frac{r_i}{\lambda} \right) \right], \quad (10)$$

where  $r_i = (x_i^2 + y_i^2 + z_i^2)^{1/2}$ , while the Newtonian acceleration is given by

$$a_x^N = \sum_i \frac{Gm_i x_i}{r_i^3}, \quad (11)$$

where the subscript  $i$  refers to a particular voxel in the mass distribution. Figure 10 shows parametric curves for which Eq. (8) would be satisfied for our device, along with the present limits from [18–20]. We predict a  $2\sigma$  statistical constraint on  $\alpha$  of  $8 \times 10^{-3}$  with this apparatus. This suggests that this experiment is currently within a factor of 6 of improving the limits on  $\alpha$  near  $\lambda = 20$  cm.

In future experiments, significant improvements to this constraint are possible. We explore this by highlighting an optimized source mass geometry. To begin, we note that the constraint is limited by the weakest of the two signals,  $a_1$  and  $a_2$ , since the acceleration uncertainty is absolute. In an experiment of this type, it is common practice to increase the source mass with increasing distance, to mute this effect [38]. Furthermore, we consider an enhanced gravitational signal due to increased source mass density (tungsten instead of lead) and reduced proximity. The proposed setup is shown in Fig. 11. We choose a cylindrical source mass geometry to allow derivation of an analytic model. For simplicity, this analysis assumes the ensemble is stationary in time.

We use a bounded minimum search to find optimal values for all parameters shown in Fig. 11. These values are listed in Table I for three chosen cases: a mass limit of 1000 kg with a nearest approach of  $d_1 = 1$  cm, and a mass limit of 5000 kg with a nearest approach of  $d_1 = 1$  and 0.1 cm. The results of these

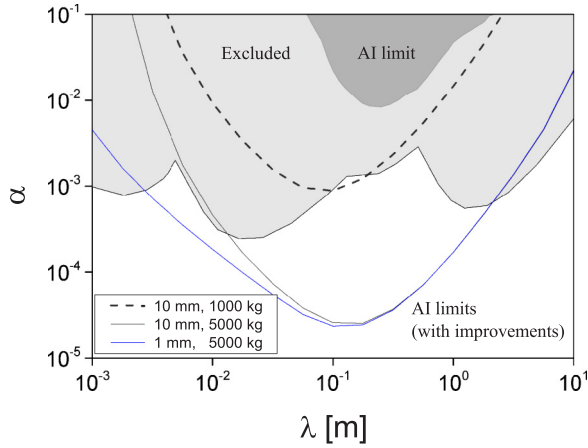


FIG. 10. (Color online) Statistical atom interferometer (AI) Yukawa constraint using  $2\text{-}\sigma$  confidence bounds (shaded dark gray) is compared with the present limits from [18–20] (shaded light gray). This apparatus could be used to constrain  $\alpha$  at the  $8 \times 10^{-3}$  level for  $\lambda$  near 20 cm. Three forecast curves are shown for the tungsten configurations detailed in Table I. With upgrades to the test mass configuration, the demonstrated sensitivity can exceed current limits with a source-to-atom distance of 10 mm and mass of 1000 kg. Achieving atom shot-noise limited sensitivity and increasing the mass to 5000 kg predicts limits approaching the  $10^{-5}$  level for source-to-atom distances of 10 and 1 mm (see Fig. 11).

projections are shown in Fig. 10. We note that the prediction for configuration A is readily achievable using an optimized geometry with the demonstrated sensitivity of the apparatus.

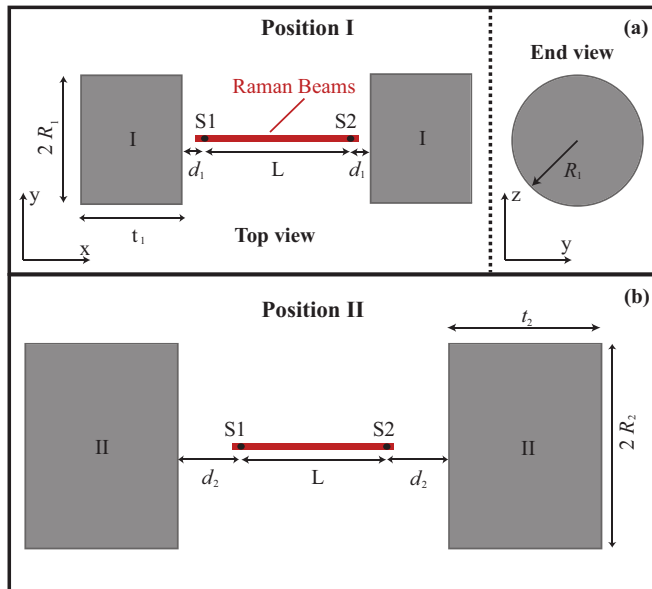


FIG. 11. (Color online) Proposed cylindrical mass configuration for an improved ISL measurement. The source mass positions alternate between a null position and configuration I or II, (a) and (b), respectively. The parameter  $d_1$  represents the distance of closest approach to the atoms and  $L$  is chosen to be much larger than the spatial extent of the source masses. Parameter values are given in Table I for three configurations.

TABLE I. Optimized tungsten source mass parameters for proposed ISL tests in Fig. 11 found by limiting the nearest source-mass-to-atom ensemble distance to either 0.1 or 1.0 cm, and limiting the largest mass to either 1000 or 5000 kg. Predictions using these parameters are shown in Fig. 10.

Configuration		A	B	C
Position I	$d_1$ [cm]	1.0	1.0	0.1
	$t_1$ [cm]	12.7	21.5	21.3
	$R_1$ [cm]	13.6	22.5	21.4
	$m_1$ [kg]	117	660	588
Position II	$d_2$ [cm]	15.0	24.3	22.4
	$t_2$ [cm]	26.3	45.3	45.8
	$R_2$ [cm]	25.1	42.7	42.5
	$m_2$ [kg]	1000	5000	5000

Plotted also are the constraints achievable using configurations B and C, and our demonstrated atom shot-noise limited detection [27]. Reducing the atom-mass proximity to  $d_1 = 0.1$  cm significantly extends the constraint to shorter  $\lambda$ . Further avenues for improvement as discussed in Sec. VA apply equally here, prompting forecast exclusions of  $\alpha$  below  $10^{-5}$ .

Bringing the source to a distance of 0.1 cm from the atoms represents a significant experimental challenge, as this is equivalent to the size of the cloud in the current apparatus. However, recent progress in atomic fountains has demonstrated atom cooling and launch techniques that can be modified to achieve high localization and low expansion [39]. Recent theoretical work indicates that further refinements can provide a measurement at the 10-cm length scale exceeding well beyond the  $10^{-5}$  level [40]. At this proposed precision level, many sources of error can limit the accuracy. Possibilities include edge effects from the finite source mass extent, surface flatness, and launch angle with respect to the source mass surface. Furthermore, the extended baseline of  $L \gg 1$  m will place an additional constraint on the frequency stability of the Raman laser which scales with baseline. Refinements to both the source mass and source mass modeling will be necessary for these measurements.

## VI. CONCLUSION

We have presented here a horizontal gravity gradiometer for precision gravitational tests. Using this apparatus, we have demonstrated a statistical uncertainty of  $3 \times 10^{-4}$  for a proof-of-concept measurement of the gravitational constant that is competitive with the present limit of  $1.2 \times 10^{-4}$ . Improvements can enable uncertainties falling well below  $10^{-5}$ . We have also interpreted this work as a constraint on a Yukawa-type fifth force and project a  $10^2$  improvement over current known constraints near  $\lambda = 10$  cm. The horizontal configuration offers the potential for superior tests of gravitational physics. The free-fall nature of the atom interferometer technique benefits from maximizing the inertially relevant dwell time of the atoms near the proof mass. As a result, a surface oriented normal to gravity and probed in the same direction will achieve this goal. However, this approach presents a new challenge in implementation, namely, a first-order sensitivity to Raman laser beam steering, which couples to the signal from

earth's gravitational force. We have shown that evacuation of the Raman beam path overcomes this challenge. We also clearly show the importance of stabilization of the Raman laser frequency for low phase-noise measurements with meter-scale baselines. Incorporating the former into a reimagined test mass geometry as well as reducing the separation of the atoms and the proof masses can result in a significant improvement to our knowledge of gravity.

## ACKNOWLEDGMENTS

We are indebted to Kai Bongs, Matt Cashen, Jeff Fixler, Todd Gustavson, Ken Takase, and Brent Young for countless contributions to the design and construction of the apparatus. This work was supported by AFRL under Contract No. F19628-02-C-0096 and DARPA under Contract No. W911NF-06-1-0064.

- 
- [1] J. B. Fixler, G. T. Foster, J. M. McGuirk, and M. A. Kasevich, Atom interferometer measurement of the Newtonian constant of gravity, *Science* **315**, 74 (2007).
- [2] G. Rosi, F. Sorrentino, L. Cacciapuoti, M. Prevedelli, and G. M. Tino, Precision measurement of the Newtonian gravitational constant using cold atoms, *Nature (London)* **510**, 518 (2014).
- [3] J. M. McGuirk, G. T. Foster, J. B. Fixler, M. J. Snadden, and M. A. Kasevich, Sensitive absolute-gravity gradiometry using atom interferometry, *Phys. Rev. A* **65**, 033608 (2002).
- [4] L. P. Parazzoli, A. M. Hankin, and G. W. Biedermann, Observation of free-space single-atom matter wave interference, *Phys. Rev. Lett.* **109**, 230401 (2012).
- [5] D. S. Durfee, Y. K. Shaham, and M. A. Kasevich, Long-term stability of an area-reversible atom-interferometer Sagnac gyroscope, *Phys. Rev. Lett.* **97**, 240801 (2006).
- [6] H. J. McGuinness, A. V. Rakholia, and G. W. Biedermann, High data-rate atom interferometer for measuring acceleration, *Appl. Phys. Lett.* **100**, 011106 (2012).
- [7] D. L. Butts, J. M. Kinast, B. P. Timmons, and R. E. Stoner, Light pulse atom interferometry at short interrogation times, *J. Opt. Soc. Am. B* **28**, 416 (2011).
- [8] R. Geiger, V. Ménot, G. Stern, N. Zahzam, P. Cheinet, B. Battelier, A. Villing, F. Moron, M. Lours, Y. Bidel, A. Bresson, A. Landragin, and P. Bouyer, Detecting inertial effects with airborne matter-wave interferometry, *Nat. Commun.* **2**, 474 (2011).
- [9] A. V. Rakholia, H. J. McGuinness, and G. W. Biedermann, Dual-axis high-data-rate atom interferometer via cold ensemble exchange, *Phys. Rev. Applied* **2**, 054012 (2014).
- [10] S. Dimopoulos, P. W. Graham, J. M. Hogan, and M. A. Kasevich, Testing general relativity with atom interferometry, *Phys. Rev. Lett.* **98**, 111102 (2007).
- [11] D. Schlippert, J. Hartwig, H. Albers, L. L. Richardson, C. Schubert, A. Roura, W. P. Schleich, W. Ertmer, and E. M. Rasel, Quantum test of the universality of free fall, *Phys. Rev. Lett.* **112**, 203002 (2014).
- [12] P. W. Graham, J. M. Hogan, M. A. Kasevich, and S. Rajendran, New method for gravitational wave detection with atomic sensors, *Phys. Rev. Lett.* **110**, 171102 (2013).
- [13] P. J. Mohr, B. N. Taylor, and D. B. Newell, CODATA recommended values of the fundamental physical constants: 2010, *Rev. Mod. Phys.* **84**, 1527 (2012).
- [14] A. P. Mills, Proposed null experiment to test the inverse square nature of gravitation, *Gen. Relativ. Gravit.* **11**, 1 (1979).
- [15] G. T. Gillies, The Newtonian gravitational constant: Recent measurements and related studies, *Rep. Prog. Phys.* **60**, 151 (1997).
- [16] K. Kuroda, Anelasticity in  $G$  experiments, *Meas. Sci. Technol.* **10**, 435 (1999).
- [17] E. G. Adelberger, B. R. Heckel, and A. E. Nelson, Tests of the gravitational inverse-square law, *Annu. Rev. Nucl. Part. Sci.* **53**, 77 (2003).
- [18] J. K. Hoskins, R. D. Newman, R. Spero, and J. Schultz, Experimental tests of the gravitational inverse-square law for mass separations from 2 to 105 cm, *Phys. Rev. D* **32**, 3084 (1985).
- [19] M. V. Moody and H. J. Paik, Gauss's law test of gravity at short range, *Phys. Rev. Lett.* **70**, 1195 (1993).
- [20] S.-Q. Yang, B.-F. Zhan, Q.-L. Wang, C.-G. Shao, L.-C. Tu, W.-H. Tan, and J. Luo, Test of the gravitational inverse square law at millimeter ranges, *Phys. Rev. Lett.* **108**, 081101 (2012).
- [21] *Atom Interferometry*, edited by P. R. Berman (Academic Press, San Diego, CA, 1997).
- [22] M. A. Kasevich, Atom interferometry in an atomic fountain, Ph.D. thesis, Stanford University, 1992.
- [23] K. Bongs, R. Launay, and M. A. Kasevich, High-order inertial phase shifts for time-domain atom interferometers, *Appl. Phys. B* **84**, 599 (2006).
- [24] R. P. Feynman, *Quantum Mechanics and Path Integrals* (McGraw-Hill, New York, 1965).
- [25] G. W. Biedermann, Gravity tests, differential accelerometry and interleaved clocks with cold atom interferometers, Ph.D. thesis, Stanford University, 2007.
- [26] This temperature is partially defined by the size of the detection aperture and the size of the detection laser beam due to the mapping of atom velocity to atom position at the end of the fountain. From alternative measurements and theory we calculate a cloud temperature of  $7 \mu\text{K}$  following launch.
- [27] G. W. Biedermann, X. Wu, L. Deslauriers, K. Takase, and M. A. Kasevich, Low-noise simultaneous fluorescence detection of two atomic states, *Opt. Lett.* **34**, 347 (2009).
- [28] G. W. Biedermann, K. Takase, X. Wu, L. Deslauriers, S. Roy, and M. A. Kasevich, Zero-dead-time operation of interleaved atomic clocks, *Phys. Rev. Lett.* **111**, 170802 (2013).
- [29] A. Peters, K. Y. Chung, and S. Chu, High-precision gravity measurements using atom interferometry, *Metrologia* **38**, 25 (2001).
- [30] G. T. Foster, J. B. Fixler, J. M. McGuirk, and M. A. Kasevich, Method of phase extraction between coupled atom interferometers using ellipse-specific fitting, *Opt. Lett.* **27**, 951 (2002).
- [31] R. W. Fox, C. W. Oates, and L. W. Hollberg, in *Cavity-Enhanced Spectroscopies: Experimental Methods in the Physical Sciences*, edited by R. D. Van Zee and J. P. Looney (Academic, San Diego, CA, 2002).
- [32] J. K. Stockton, X. Wu, and M. A. Kasevich, Bayesian estimation of differential interferometer phase, *Phys. Rev. A* **76**, 033613 (2007).
- [33] N. Bobroff, Recent advances in displacement measuring interferometry, *Meas. Sci. Technol.* **4**, 907 (1993).

- [34] J. Le Gouët, P. Cheinet, J. Kim, D. Holleville, A. Clairon, A. Landragin, and F. P. Dos Santos, Influence of lasers propagation delay on the sensitivity of atom interferometers, *Eur. Phys. J. D* **44**, 419 (2007).
- [35] F. Sorrentino, Q. Bodart, L. Cacciapuoti, Y.-H. Lien, M. Prevedelli, G. Rosi, L. Salvi, and G. M. Tino, Sensitivity limits of a Raman atom interferometer as a gravity gradiometer, *Phys. Rev. A* **89**, 023607 (2014).
- [36] J. M. McGuirk, M. J. Snadden, and M. A. Kasevich, Large area light-pulse atom interferometry, *Phys. Rev. Lett.* **85**, 4498 (2000).
- [37] S.-W. Chiow, T. Kovachy, H.-C. Chien, and M. A. Kasevich,  $102\hbar k$  large area atom interferometers, *Phys. Rev. Lett.* **107**, 130403 (2011).
- [38] E. Fischbach and C. L. Talmadge, *The Search for Non-Newtonian Gravity* (Springer-Verlag, New York, 1999).
- [39] S. M. Dickerson, J. M. Hogan, A. Sugarbaker, D. M. S. Johnson, and M. A. Kasevich, Multiaxis inertial sensing with long-time point source atom interferometry, *Phys. Rev. Lett.* **111**, 083001 (2013).
- [40] J. G. Wacker, Using atom interferometry to search for new forces, *Phys. Lett. B* **690**, 38 (2010).